Available online at www.sciencedirect.com
SCIENCE DIRECT®
International Journal of Heat and Mass Transfer 48 (2005) 691–701
International Journal of HEAT and MASS TRANSFER
www.elsevier.com/locate/ijhmt

Flow characteristics and heat transfer performances of a semi-confined impinging array of jets: effect of nozzle geometry

Bertrand P.E. Dano [a], James A. Liburdy [a,*], Koonlaya Kanokjaruvijit [b]

[a] Department of Mechanical Engineering, Oregon State University, 204 Rogers Hall, Corvallis, OR 97331 6001, USA
[b] Department of Mechanical Engineering, Imperial College, London, England

Received 11 September 2003; received in revised form 4 June 2004
Available online 11 November 2004

Abstract

The flow and heat transfer characteristics of confined jet array impingement with crossflow is investigated. Discrete impingement pressure measurements are used to obtain the jet orifice discharge flow coefficient. Digital particle image velocimetry (DPIV) and flow visualization are used to determine the flow characteristics. Two thermal boundary conditions at the impinging surface are presented: an isothermal surface, and a uniform heat flux, where thermocouple and thermochromic liquid crystal methods were used, respectively, to determine the local heat transfer coefficient. Two nozzle geometries are studied, circular and cusped ellipse. Based on the interaction with the jet impingement at the surface, the crossflow is shown to influence the heat transfer results. The two thermal boundary conditions differ in overall heat transfer correlation with the jet Reynolds number. Detailed velocity data show that the flow development from the cusped ellipse nozzle affects the wall region flow more than the circular nozzle, as influenced by the crossflow interactions. The overall heat transfer for the uniform heat flux boundary condition is found to increase for the cusped ellipse orifice.

Keywords: Impinging jets; Array; Non-axisymmetric nozzle; Impinging heat transfer; DPIV

1. Introduction

In a general review, Margason [1] indicates that jets in crossflow have been of interest for sixty years or more, but detailed studies of jet impingement with crossflow date only from the past several decades. Many engineering applications currently use jet impingement to improve the cooling over a wide range of length scales and configurations. Han and Goldstein [2] reviewed jet array impingement heat transfer techniques used in gas turbine blades. They concluded that further investigation of the combined effects of some parameters, such as the crossflow, the impingement plate ''roughness'', and the jets nozzle shape to optimize turbine blades cooling.

The use of impinging jets in industrial and electronic cooling applications evolved rapidly from a single jet to arrays of jets [3–7], thereby providing a more uniform cooling. Upon impingement, jets usually dissipate in

* Corresponding author. Tel.: +1 541 737 7017; fax: +1 541 737 2400.
E-mail addresses: dano@engr.orst.edu (B.P.E. Dano), liburdy@engr.orst.edu (J.A. Liburdy), koonlaya.kanokjaruvijit@ic.ac.uk (K. Kanokjaruvijit).

0017-9310/$ - see front matter © 2004 Elsevier Ltd. All rights reserved.
doi:10.1016/j.ijheatmasstransfer.2004.07.046

Nomenclature

A_j	individual jet orifice area
A_t	jet orifice area = NA_j
A_s	impingement surface area
C_D	jet discharge flow coefficient, $\frac{\dot{M}_{actual}}{\dot{M}_{isentropic}}$ (see Eq. (1))
D_H	jet orifice hydraulic diameter
h	surface heat transfer coefficient
$\bar{h}$	surface average heat transfer coefficient
H	jet array to impingement plate distance
$\dot{M}_{actual}$	actual mass flow rate
$\dot{M}_{isentropic}$	ideal mass flow rate (isentropic)
N	number of jets
Nu	average Nusselt number, $\frac{\bar{h}D_H}{k_{air}}$
P	pressure
q_{in}	energy input
q_{out}	energy output, $\bar{h}A_s(T_s - T_j)$
T	temperature
X	distance along the impingement surface, centered under each jet
Y	distance from the impingement surface
Re	Reynolds number, $\frac{V_j D_H}{\nu}$
V_c	average crossflow velocity at a particular crossflow position
V_j	average jet velocity
V_r	velocity ratio, V_c/V_j
Z	spanwise distance along the plate

Greek symbols

ν	kinematic viscosity of air
ρ	density of air

Subscripts

0	plenum chamber
j	jet
s	impingement surface
iso	isothermal surface
uhf	uniform heat flux surface

all directions, but when arranged in an array with sidewall constraints, a directed crossflow results. In particular, three sidewalls create a crossflow with increasing strength towards the flow exhaust.

Crossflows have been found to influence the jet flow structure. Florschuetz and Isoda [8] measured the pressure drop across circular orifices of a jet array. The discharge flow coefficient, C_D, was found to decrease with increasing crossflow. Using laser-Doppler velocimetry, Barata and co-workers [9] and [10] showed that the flow pattern for each jet is similar to a single impinging jet but gives rise to a fountain upwash which interacts with the crossflow. They highlighted the presence of a complex three-dimensional "scarf" vortex around each impinging jet. Using a combination of flow visualization and laser-Doppler velocity measurement Benard et al. [11] described the fluid behavior in the vicinity of the plane wall, and proposed a topology of the flow including a ground vortex structure.

In the last decade, local heat transfer measurement on surfaces has been highly facilitated by the use of thermochromic liquid crystal paints and films [12–18] These studies have provided extensive results on the spatial distribution of the surface temperature and have assessed surface heat transfer conditions. Of the many parameters inherent to jet array heat transfer, the jet-to-jet spacing and impingement distance have been extensively studied. Hamadah [19] showed that the maximum heat transfer coefficient occurres between a jet spacing of 2 and 4 jet diameters. Without crossflow effect, Huber and Viskanta [20] found that the maximum Nusselt number (Nu) does not occur at the stagnation point, but at secondary rings formed around the stagnation point. These secondary rings increase the spatially averaged heat transfer coefficient. At lower Reynolds numbers (Re) and increased nozzle-plate distance, they observed that the magnitude of the inner secondary peak decreases. Their results can be summarized by the following correlation: $\overline{Nu} = 0.285Re^{0.710}Pr^{0.33}(H/D)^{-0.123} \times (X_n/D)^{-0.725}$ as a function of the following thermo-physical parameters: Re is the Reynolds number, Pr is the Prandtl number, H is the distance between the orifice plate and the impingement surface, X_n is the distance between jets in a square array and D is the jet diameter. Schroeder and Garimella [21] found that the peaks of local heat transfer coefficients for a 9×9 jet array without crossflow are near the centers of the impinging jets, and that the average heat transfer coefficient was nearly twice that of a single jet. They showed that when the ratio of impingement distance to jet diameter decreases, the heat transfer coefficient increases. Moreover, this effect is stronger at higher Reynolds numbers. Their results can be summarized by the following correlation: $\overline{Nu} = 0.127Re^{0.693}Pr^{0.4}(H/D_H)^{-0.105}$ which is valid for $5000 \leqslant Re \leqslant 20{,}000$, $0.5 \leqslant H/D_H \leqslant 4$. Obot and Trabold [22] studied the jet induced crossflow effects for three flow configurations: unrestricted, restricted on two sides and restricted on three sides. In the last configuration, the crossflow strength increases from the back towards the exhaust. They found that the local Nusselt number is higher where the crossflow is the weakest and that the unrestricted case was the best configuration

for impingement cooling. Their model for the restricted channel on three sides can be summarized by the following correlation: $\overline{Nu} = 0.032Re^{0.8}(H/D)^{-0.28}$.

Metzger [23], in a crossflow configuration, found that large orifice spacing and small impingement distance are favorable for uniform heat transfer distribution. They explained that large impingement distance and smaller hole spacing tend to let the jet diffuse in the crossflow resulting in a reduction of cooling efficiency due the confinement of the spent air forced to become "channelized" between adjacent streamwise rows of jets. Their results can be summarized by the following correlation: $Nu = ARe_j^m\{1 - B[(z/D)(G_c/G_j)]^n\}Pr^{1/3}$ where $A, m, B, n = C(x_n/D)^{n_x}(y_n/D)^{n_y}(z/D)^{n_z}$, C, n_x, n_y, n_z are constants, x_n is the streamwise jet hole spacing, y_n is the spanwise jet hole spacing, z is channel height, G_c is the crossflow mass velocity based on channel cross-sectional area, and G_j is the jet mass velocity based on jet hole area.

The heat transfer effects by various modifications to the flow field have been examined. Rhee et al. [24] studied the effect of effusion holes located adjacent to the jets, on the crossflow. They found that even though the heat transfer at the stagnation regions is enhanced by the crossflow, a more uniform heat transfer distribution can be obtained with effusion holes. In addition, an increase of the average heat transfer of up to 60% was shown for impingement distances less than two jet diameters, due to the evacuation of spent air. Huang et al. [25] studied the effects of various modifications of the impingement surface on the heat transfer. Their results show that some improvement (up to 20%) can be obtained with dimples, pins or effusions holes. Also, Parsons and Han [26] showed that static tests tend to over-predict the heat transfer coefficients results by a factor of 15–20% compared to the results with rotation and the effect of rotation in the case of gas turbine blade cooling.

The effect of longitudinal fins on the impingement surface using impinging jets with added forced crossflow was studied by Failla et al. [27]. Their results show that for the same flow rate, an increase of as much as 220% compared to pure jet impingement can be obtained due to the crossflow.

Several studies have looked at the impact of non-circular jets. Lee et al. [28] investigated local heat transfer distribution, for an elliptical jet impinging on a constant heat flux surface, using thermochromic liquid crystals. They found that the isothermal surface contours change in shape from elliptic to near circular, back to elliptic again with increasing jet-to-surface distance. The heat transfer coefficient for the elliptical jet at the stagnation point was found to be 10% higher than a circular jet. Owens and Liburdy [29] demonstrated that using an elliptic jet at low Reynolds numbers improves the average heat transfer up to 37% over a circular jet. Arjocu and co-workers [30–32] showed that at higher impingement distances, the elliptic jet streamlines converge in the major axis planes while they spread in the minor axis plane. This behavior is typical of non-axisymmetric jet orifices and is part of the "axis switching" process. The axis switching superimposed on the jet column instability, swaying motion, and presence of small-scale shear layer structures leads to a high level of turbulence and entrainment in the impingement region, which is generally thought to enhance surface cooling.

The objective of this paper is to provide a better understanding of the mean flow characteristics and heat transfer of jet array impingement with crossflow, using different jet orifice geometries: circular and cusped ellipse. The latter jet orifice is oriented with either its major or minor axis aligned with the crossflow. Also, both isothermal and constant heat flux boundary conditions at the impingement surface are studied. The results are divided as follows: a general overview of the jet flow and the surface temperature distribution, the flow coefficient characteristics along with the average velocity and vorticity, and finally, the surface heat transfer characteristics along with a discussion relative to the flow conditions and finally a summary.

2. Experimental setup and method

Experiments were designed to study both the jet impingement crossflow interaction as well as the surface heat transfer. In addition, the heat transfer was studied using both a uniform temperature and a uniform heat

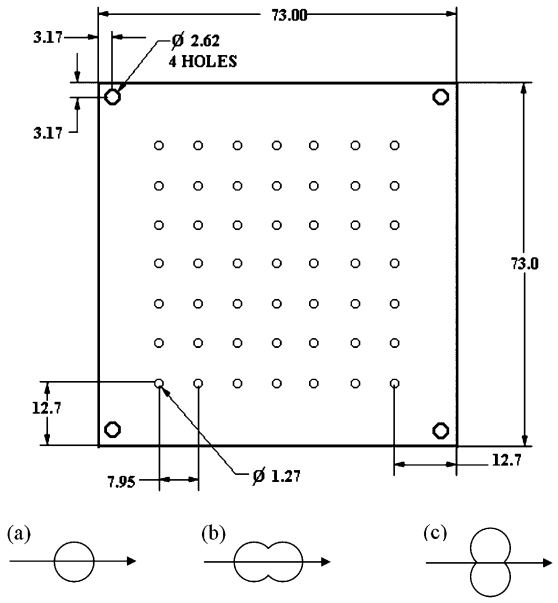

Fig. 1. Jet array geometry and orifice geometry: (a) circular jet, (b) cusped ellipse (0°), (c) cusped ellipse (90°).

flux impingement boundary condition. The orifice plate and jet geometries used in this study are shown in Fig. 1. Both orifice shapes are designed to have the same cross-sectional flow area: $A = 1.267 \times 10^{-6}\,\mathrm{m}^2$, and therefore slightly different hydraulic diameters: D_H of circular orifice is 1.27×10^{-3} m and D_H of cusped ellipse is 1.138×10^{-3} m. Two sets of circular and cusped ellipse jet arrays were used. One was made of 1 mm thick stainless steel, and the second was made of 1.24 mm thick quartz, to allow direct viewing of the impingement surface. The sensitivity to different parameters such as the impingement distance, $H/D_H = 2$–4, Reynolds number, $Re = 8500$–15,900, and cusped ellipse nozzle orientation are investigated. When the major axis of the cusped ellipse is aligned with the crossflow, it is noted as 0° and when aligned normal to the crossflow, it is noted as 90°, as shown in Fig. 1.

The test facility consisted of a stainless steel cubic plenum chamber (30 cm side length) with the jet orifice plate at the bottom of the chamber and the impingement surface fastened directly below the jet array. A pressure-regulated dry-air compressor supplied air to the plenum chamber in which a diffuser plate was installed, providing a volume of air at high pressure and low velocity above the jet orifice plate. The impingement surface was surrounded by three Plexiglas walls, which together with the impingement surface formed an exhaust flow channel. The jet flow impinged on the bottom plate and escaped out the open side into ambient conditions.

The flow exhaust created a crossflow, which increased in magnitude along the flow direction. The total mass flow rate was evenly divided among the 49 jets with less than a 2% variation of dynamic pressure as measured at each orifice exit. The crossflow velocity, V_c, increases in the downstream direction with the crossflow average velocity based on the total flow from all upstream jets and the crossflow cross-sectional area, which is normal to the crossflow direction. The crossflow-to-jet velocity ratio is defined as $V_r = V_c/V_j$, where V_j is the average exit velocity of the jets. V_r is independent of jet Reynolds number but increases with the downstream location and is a linear function of the jet position along the flow direction. The rate of increase of V_r along the flow direction is greater for smaller impingement distance, H/D_H. Velocity ratios range from 0 to 0.382 for $H/D_H = 2$ and from 0 to 0.191 for $H/D_H = 4$.

Five different impingement plate assemblies were designed to study the following: surface pressure distribution, surface flow visualization, flow field (using DPIV), isothermal heat transfer, and uniform heat flux heat transfer. In Fig. 2 three schematics of the impingement plate assembly designs are shown: (a) the pressure plate and the DPIV fields of view, (b) the isothermal heat transfer plate, and the uniform heat flux plate. The pressure drop through the jet orifice was measured using a special impingement plate with five pressure taps placed

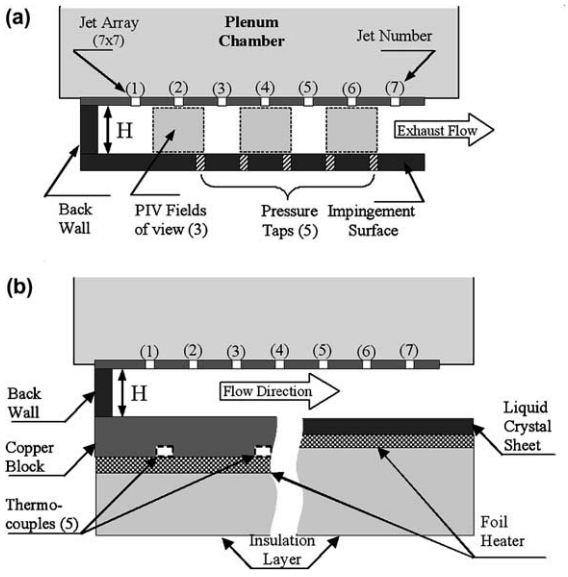

Fig. 2. Impingement plate setup: (a) pressure and DPIV, (b) left: uniform temperature; right: uniform heat flux.

midway between each centerline jet location. In addition, two pressure taps were placed along the central spanwise rows to detect symmetry across a row of jets. The latter two were also used to align the impingement plate. Pressure data were used to determine the flow coefficient, C_D, of the jets and its variation along the flow. The flow coefficient, C_D, for an individual jet was obtained using the isentropic gas dynamic laws for flow through an orifice as used by Florschuetz and Isoda [8]

$$C_D = \frac{\frac{\dot{M}_{actual}}{A_t}}{P_0\left(\frac{P_s}{P_0}\right)^{\frac{1}{\gamma}}\sqrt{\frac{2\gamma}{R\cdot T_0(\gamma-1)}\cdot\left[1-\left(\frac{P_s}{P_0}\right)^{\frac{\gamma-1}{\gamma}}\right]}} \quad (1)$$

Impingement plate flow visualization was obtained by heavily seeding the jet flow with nominally 2.5 μm diameter TiO_2 particles. Local deposition of the seed on the impingement surface provided a signature of the average flow pattern near the surface of the impingement plate.

Digital particle image velocimetry (DPIV) was performed using a double pulse Nd:YAG laser. The optic system provided a thin laser sheet (1 mm thick) aligned with a designated row of jets along the crossflow direction. The jet flow was seeded with 2.5 μm TiO_2 particles and the flow impinged on a clear Plexiglas plate. A digital camera was positioned perpendicular to the laser sheet, viewing through one transparent sidewall. Pairs of high-resolution pictures were recorded (1300×1030 pixels) with a 2 μs time separation. The velocity flow field was obtained using cross-correlation analysis on the pairs of pictures, yielding the near instantaneous velocity

field of the flow. The DPIV interrogation sub-region was 128 pixels with a 75% overlap, providing a vector-to-vector spacing of 200 μm. Over 50 instantaneous velocity flow fields were obtained for each jet and then averaged to highlight the mean flow structure. From the velocity flow field the vorticity field was obtained, using a centered finite difference scheme. The locations of the DPIV fields are shown in Fig. 2a. Further details of flow measurements can be found in Dano [33].

Isothermal heat transfer characteristics were obtained using a heated copper block with an array of five surface embedded thermocouples. A foil heater placed between the copper block and a Plexiglas insulation block provided heating. The surface temperature was maintained uniform to within ±3.2 °C. Heat losses through the insulation were calculated to be less than 1.5% of the total heat input. The surface average heat transfer coefficient was calculated from the measured heat input less losses and is based on the temperature difference between plenum and impingement surface. The uncertainty on the Nu for the isothermal heat transfer case was between 3% and 7%.

The uniform heat flux characteristics were obtained using a cholesteric liquid crystal sheet manufactured by Hallcrest™. A color CCD camera (640 × 480 pixels) was used to acquire images of the impingement surface through a window in the plenum chamber and through the quartz orifice plate using a 45° inclined mirror positioned in the plenum. The color changes were calibrated based on the measured hue values versus the corresponding temperature over the full temperature range of the liquid crystal (5 °C). The local heat transfer coefficient distribution was calculated based on the known heat flux provided by the foil heater and the local surface temperature minus jet plenum temperature. The uncertainty of $\overline{Nu}$ for the uniform heat flux heat transfer case was below 4%. Further details of the heat transfer measurements are given by Kanokjaruvijit [34].

3. Results

3.1. General flow and local temperature pattern

The general flow pattern at the surface of the impingement plate can be observed from the surface flow visualization and the uniform heat flux measurement images shown in Fig. 3. Both results illustrate an array of cells with a characteristic "horseshoe" shape around the impingement point. Along the spanwise direction, the results are periodic indicating the symmetry plane between jet rows. Each cell appears to be defined by four detachment–reattachment zones. The upstream part of the horseshoe occurs at the stagnation zone created by the crossflow and the jet flow that is directed upstream after impingement. The side legs of the horseshoe are due to the roll-up of adjacent jets creating a flow channeled between the rows of jets. A black and white reconstruction of the color image representing the temperature is also shown in Fig. 3. Comparing the surface flow visualization and surface temperature mapping, the stagnation point appears to correspond to the lowest temperature. The highest temperature is observed in the channeled flow area, between rows. As the jet-to-crossflow ratio, V_r, increases (i.e., moving downstream from the back towards the exhaust), it is observed that the "horseshoe" configuration of the cells become increasingly more oblong in shape. For jets closer to the back wall, the impingement point is located nearly at the center of each cell. With increasing V_r, the boundaries shift progressively in the downstream direction until the upstream detachment zone nearly merges with the impingement point, indicative of the increasing strength of the crossflow moving towards the exhaust. Similar imaging results were found for all the different jet array configurations by Dano [33].

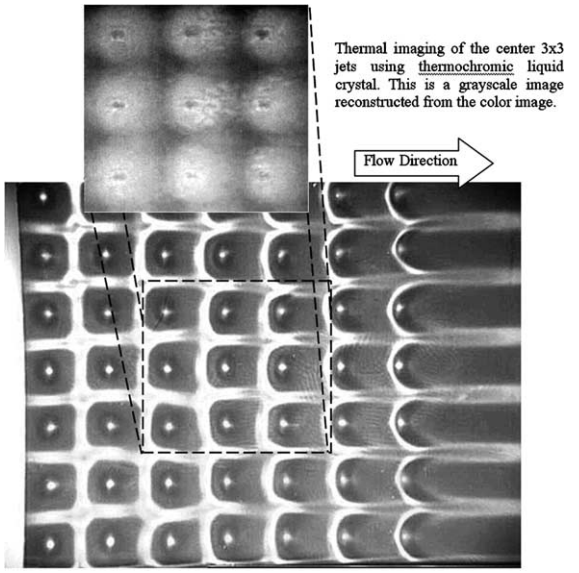

Fig. 3. Surface flow visualization using TiO_2 micron-size particles; dashed line represents the area of surface temperature mapping.

3.2. Discharge flow coefficient characteristics

Results of C_D for impingement distance of $H/D_H = 2$ and 4 for various values of Re, and for both jet geometries are provided in Figs. 4 and 5. As the jet-to-crossflow ratio increases along the downstream crossflow direction, the flow coefficient, C_D, decreases slightly. The average flow coefficient over all locations is approximately 0.70 for the circular jet and 0.80 for the cusped ellipse (for both orientations, 0° and 90°). Decreasing

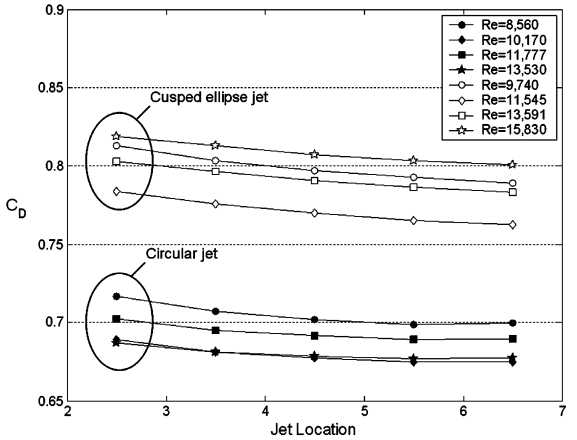

Fig. 4. Flow coefficient versus the downstream location for $H/D_H = 4$; cusped ellipse jet: open markers, circular jet: full markers.

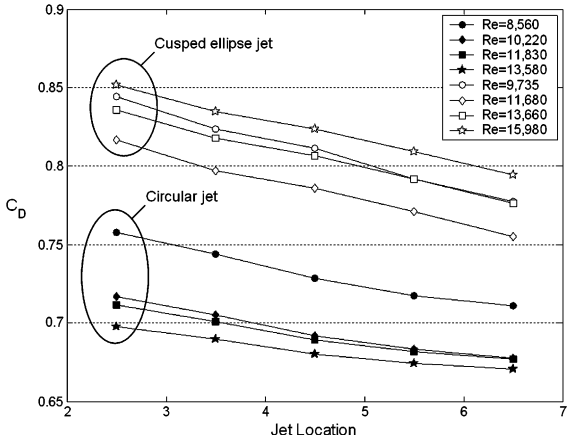

Fig. 5. Flow coefficient versus the downstream location for $H/D_H = 2$; cusped ellipse jet: open markers, circular jet: full markers.

the impingement distance, H/D_H, results in a more rapid decline of C_D in the flow direction. This is most likely a consequence of an increase in the crossflow velocity as the effective crossflow area decreases. For increasing values of Re, a slight and uniform drop of C_D, up to 5%, can be observed for all jet locations over the range of Reynolds numbers studied.

3.3. Average velocity and vorticity fields

The mean velocity flow fields obtained from the DPIV data provide detailed information about the structure of the flow. A typical example is shown in Fig. 6, for the circular jet array at jet 6 location and for $Re = 9760$. Along the centerline aligned with the

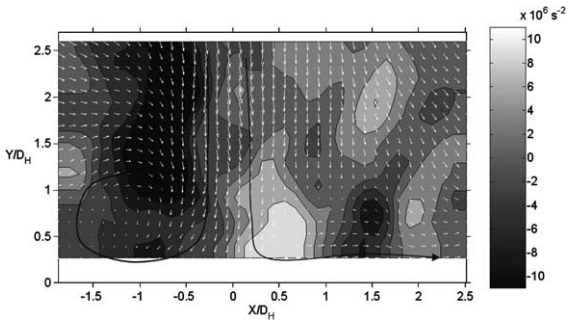

Fig. 6. DPIV measured mean velocity and vorticity flow fields for the circular jet; $H/D_H = 4$, jet 6, $V_r = 0.159$, $Re = 9790$.

crossflow, each jet appears to split into a downstream flow and an upstream flow. This upstream flow interacts with the flow coming from the upstream jet(s) to create a large recirculation region or a surface vortex. At this lower Re, the jet seems to divide evenly between upstream and downstream flow. The downstream flow resembles a stagnation flow along the impingement surface until it eventually interacts with the next downstream jet. The cusped ellipse (0°) appears to have a flow structure comparable with the circular jet. Further downstream in the jet array, as V_r increases, the surface vortex decreases in size from the height of the entire channel to about one half of the channel height, while the magnitude of velocities within the vortex increase. Also, the center of rotation stays near the impingement surface and moves progressively closer to the jet column, which is consistent with the surface flow visualization results. Increasing Re is shown to strengthen the surface vortex but does not alter the overall flow pattern, except close to the exhaust.

The mean velocity flow fields at the jet 6 location for the circular and cusped ellipse (0°) jets are shown in Figs. 7 and 8, for $H/D_H = 4$, $Re = 15{,}800$ and $Re = 13{,}500$, respectively. Results at other jets locations show similar trends. Comparing Figs. 6 and 7 for the circular jet shows that the surface vortex for the higher Re case strongly

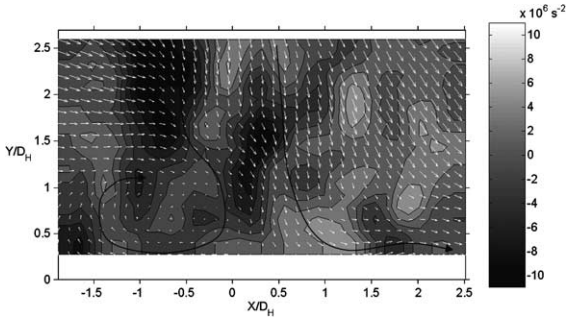

Fig. 7. DPIV measured mean velocity and vorticity flow fields for the circular jet; $H/D_H = 4$, jet 6, $V_r = 0.159$, $Re = 15{,}800$.

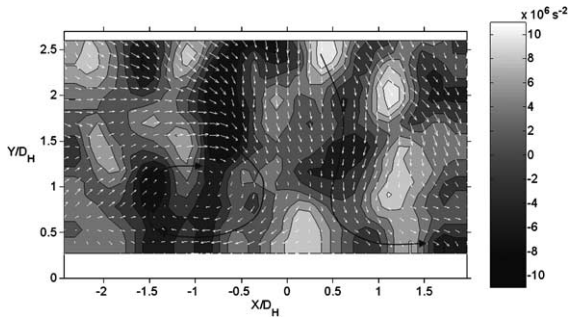

Fig. 8. DPIV measured mean velocity and vorticity fields for the cusped ellipse (0°) jet; $H/D_H = 4$, jet 6, $V_r = 0.159$, $Re = 13{,}500$.

displaces the jet column downstream, but only on the upstream side of the jet. The surface vortex size appears to expand in the streamwise direction into the jet while it shrinks somewhat in height. A larger part of the jet is deflected downstream in the case of the higher *Re* flow, and consequently the upstream vortex is made up of flow primarily from the upstream jet. Comparing Figs. 7 and 8 for the circular and cusped ellipse (0°) nozzles, respectively, shows a change on the downstream side of the jet. As the jet separates for the cusped ellipse (0°) nozzle, a contraction of the jet column is observed near $y/D_H = 1$. This contraction alters the flow near the impingement surface by generating a stronger upstream flow feeding strength to the upstream vortex and results in a larger impingement zone with higher near wall velocities. This is speculated to be caused by the axis switching phenomena mentioned previously, which typically occurs for non-axisymmetric jets between H/D_H of 3 and 4, as shown by Arjocu and Liburdy, [31]. The axis switching would also explain the observed reduction of the jet column centerline velocity, resulting from flow transfer in the transversal or spanwise direction.

The mean flow pattern for the cusped ellipse (90°) is very different from the circular and cusped ellipse (0°), as can be seen in Fig. 9. No large surface vortex is observed

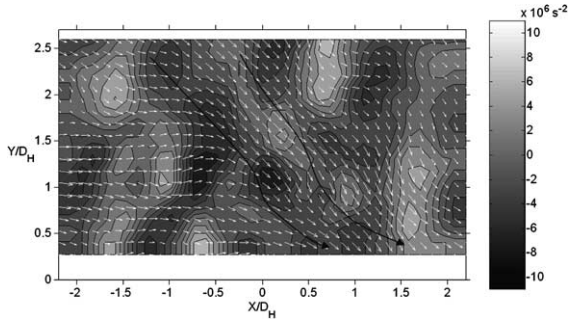

Fig. 9. DPIV measured mean velocity and vorticity fields for the cusped ellipse (90°) jet; $H/D_H = 4$, jet 6, $V_r = 0.159$, $Re = 13{,}500$.

in the mean velocity flow field at the jet location 6. However, at jet location 2, close to the back wall, there is a large and very weak recirculation structure. Although the mean velocity profiles indicate no steady vortex flow, inspection of the instantaneous velocity fields reveals a transient nature of the surface vortex for all jet locations. This vortex decays and reforms, which is presumably caused by interaction with the crossflow. Consequently, merely looking at the mean velocity field indicates no near surface vortex, but the surface flow visualization given in Fig. 3 indicate some surface upstream flow, even for the cusped ellipse (90°), which is not shown here. Refer to Dano [33] for further details.

Observation of the vorticity fields, obtained from the DPIV data provides additional information on the flow structure. Results are shown in the grayscale contours of Figs. 6–9. In Fig. 6, the jet shear layers can be located in regions of oppositely rotating vorticity on either side of the jet column. The negative vorticity along the upstream shear layer loses its strength at about $y/D_H = 1$, while the downstream shear layer strengthens near the impingement surface. The decrease of the upstream shear layer vorticity is due to the presence of the upstream vortex causing increased flow back into the jet, which reduces the strength of the shear layer. Vorticity contours for higher *Re* circular nozzle at jet location 6 are shown in Fig. 7. The surface vortex interaction with the jet column in this case is even stronger, which causes a reduction of vorticity near the upstream surface. This decrease of near surface vorticity is observed for all jet configurations at higher *Re*. Vorticity contours for the cusped ellipse orifice (0°) and (90°) at $Re = 13{,}500$ are shown in Figs. 8 and 9, respectively. Note the slight upstream shifting of the field of view compared to Figs. 6 and 7. The main distinction seen in the distributions of vorticity for the cusped ellipse (90°) is the overall reduction of vorticity. The strong upstream shear layer is reduced and the near surface vorticity levels are relatively low compared to both the circular and cusped ellipse (0°) cases. However, the cusped ellipse (0°) case has higher levels of vorticity concentrated near the stagnation point compared to the circular jet case.

3.4. Surface heat transfer characteristics

The heat transfer coefficient is presented here as both the local values and the average value expressed as Nusselt number, *Nu*. The experimental results for two limiting cases are presented: isothermal surface and uniform-flux surface. The impinging flow for the cusped ellipse (90°) is more significantly altered by the crossflow, which implies a reduced heat transfer. Consequently, because of space limitations, only the cases of the cusped ellipse (0°) and the circular jet are presented.

The average Nusselt number for the isothermal surface, Nu_{iso}, is shown in Fig. 10 for five *Re* values versus

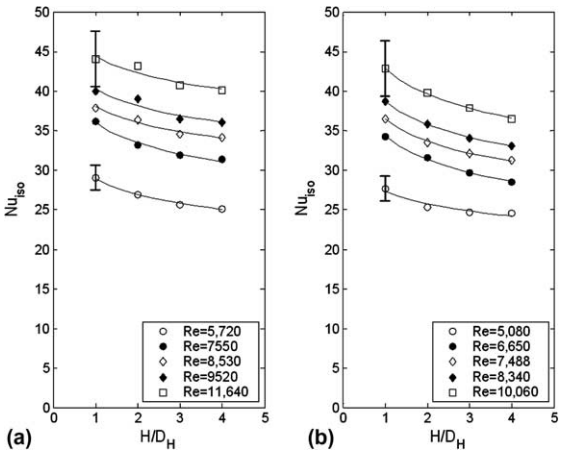

Fig. 10. Average Nusselt number for isothermal surface: (a) circular jet, (b) cusped ellipse (0°).

H/D_H for both the circular jet and the cusped ellipse (0°). For both geometries, Nu_{iso} decreases approximately 10–20% when H/D_H was increased from 1 to 4. The results show that the circular jet yields slightly higher heat transfer than the cusped ellipse (0°) jet array and the difference is larger at larger Re values. Power law fit correlations of Nu_{iso} versus Re and H/D_H for the range of data studied are

$$\text{circular jet}: Nu_{iso} = 0.1135 Re^{0.64} (H/D_H)^{-0.088} \quad (2)$$

$$\text{cusped ellipse } (0^\circ): Nu_{iso} = 0.1289 Re^{0.63} (H/D_H)^{-0.11} \quad (3)$$

for $5721 \leqslant Re \leqslant 11{,}643$ and $1 \leqslant H/D_H \leqslant 4$.

The curve fits and all of the associated data are shown in Fig. 14.

For the uniform heat flux cases, the temperature distribution measured by the liquid crystal response, coupled with the known electric energy input, was used to obtain the local heat transfer coefficient. This was then integrated over the impingement surface to calculate the surface average value, Nu_{uhf}. The maximum local heat transfer coefficient was found at the jet impingement points, and minima were found in the regions between the jets which correspond to the light areas in the flow visualization of Fig. 3, and the dark areas of the thermal image insert in Fig. 3. The distribution over the surface is similar for both nozzle geometries with peak amplitudes decreasing along the streamwise direction. This drop off produces a reduction of the overall cooling efficiency in the streamwise direction. This is presumably caused by the effect of increasing crossflow, as well as the increased heating of the crossflow in the downstream direction.

The downstream development of the local heat transfer coefficient is found to be different for the circular jet compared to the cusped ellipse (0°). This is shown in Fig. 11 by comparing the local heat transfer distribution along a line passing through the center of each jet in the crossflow direction for a representative value of Re and H/D_H. This is related to the observed difference in the jet-crossflow interaction shown in the DPIV data. In the case of the cusped ellipse (90°) there is elimination of the steady vortex upstream of impingement. For the cusped ellipse (0°) there is a focusing of the impingement flow caused by the axis switching which is aligned properly with the crossflow (in contrast to the 90° case which does not experience this focusing). The resulting increased velocity near impingement causes a slight increase in the peak heat transfer rate for the downstream jets of the cusped ellipse geometry.

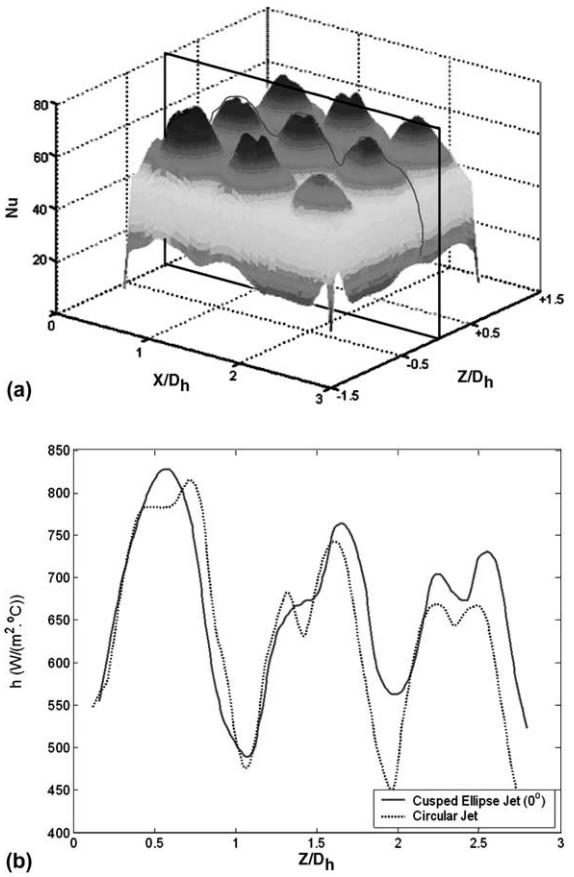

Fig. 11. (a) Isopleth of Nusselt number distribution for the cusped ellipse (0°); (b) heat transfer coefficient slice plot along the streamwise center row ($Z/D_H = 0$) for both jet geometries; $Re = 7005$, $H/D_H = 2$. (b) Average Nusselt number for uniform heat flux surface: (a) circular jet, (b) cusped ellipse (0°).

The spatially averaged Nusselt number for the uniform heat flux surface, Nu_{uhf}, versus H/D_H are shown in Fig. 12. Similar to the isothermal surface case, increasing the impingement distance decreases Nu_{uhf} by

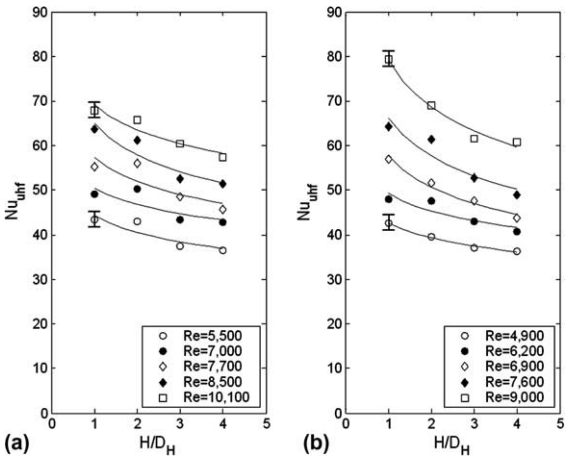

Fig. 12. Comparison to literature for circular jet isothermal surface: $Re = 5600$ and 11,500; and uniform heat flux: $Re = 5500$ and 11,500.

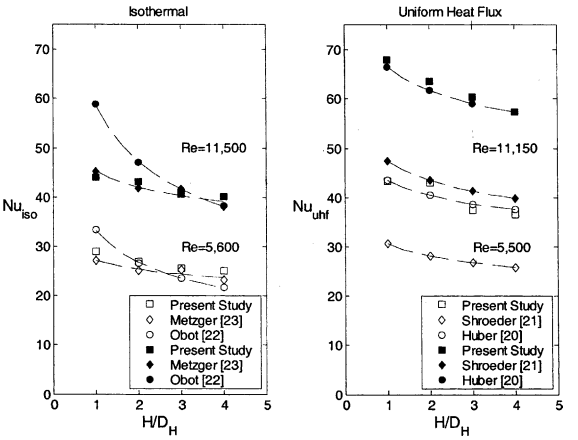

Fig. 13. Nusselt number comparison between two thermal boundary conditions at $H/D_H = 4$, for both jet geometries: (CJ) circular jet (CEO) cusped ellipse 0°, with corresponding power law curve fitting.

15–25% when H/D_H increases from 1 to 4. There is a greater difference between the two jet geometries for this thermal boundary condition, and this difference is more pronounced with increasing Re. The uniform heat flux boundary condition results indicate that the cusped ellipse (0°) improves heat transfer for higher Re values. It is also noticed that the sensitivity of Nu_{uhf} to H/D_H tends to increase with increasing Re. Power law fit correlations of Nu_{uhf} versus Re and H/D_H for each nozzle geometry, and valid for the ranges of data studied are

$$\text{circular jet}: Nu_{uhf} = 0.126 Re^{0.68} (H/D_H)^{-0.135} \quad (4)$$

$$\text{cusped ellipse } (0^\circ): Nu_{uhf} = 0.124 Re^{0.70} (H/D_H)^{-0.184} \quad (5)$$

for $5500 \leqslant Re \leqslant 10{,}100$ and $1 \leqslant H/D_H \leqslant 4$.

Compared to the isothermal boundary condition correlations given in Eqs. (2) and (3), the sensitivity of Nu_{uhf} to these two parameters, Re and H/D_H is higher for the constant heat flux boundary condition.

These results are compared to previous studies of circular jets in Fig. 13. For the isothermal surface case the data agree very well with the results of Metzger [23] rather than Obot and Trabold [22]. The latter study indicates slightly higher Nu_{iso} values at the lowest value of H/D_H. For the uniform heat flux surface case the present study agrees very well with those of Schroeder [21] but are significantly higher than those of Huber and Viskanta [20]. Reasons for this discrepancy may be that the data of Huber and Viskanta were obtained for a configuration with no crossflow and for a jet diameter five times larger, and therefore five times lower velocities.

A comparison of the average value of Nu for the two thermal boundary conditions is given in Fig. 14 for $H/D_H = 4$. Similar trends are obtained for all H/D_H values,

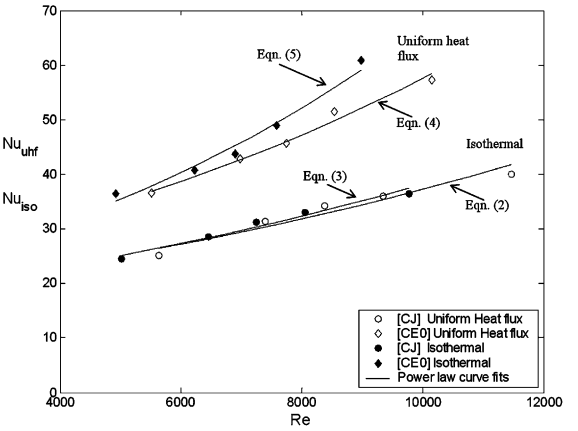

Fig. 14. Nusselt number comparison between two thermal boundary conditions at $H/D_H = 4$, for both jet geometries: (CJ) circular jet, (CEO) cusped ellipse (0°), with corresponding power law curve fitting.

where the correlations have been given previously as Eqs. (2) and (3) for the isothermal boundary condition and Eqs. (4) and (5) for the uniform heat flux condition. The uniform heat flux boundary conditions yield consistently higher heat transfer rates than does the isothermal boundary condition. The increased sensitivity of Nu to Re for the uniform heat flux case results in an increasing difference between the two surface boundary cases as Re increases. These results are consistent with those found for a number of different flow conditions. For instance, laminar flow in tubes with constant heat flux boundary conditions have a higher value of Nu for fully developed flow when the wall boundary condition

is uniform heat flux. Similarly, turbulent fully developed flow in a circular tube has higher *Nu* values for uniform heat flux, as shown in Kays [35]. The present data also indicate that the uniform heat flux case differ widely for the circular and cusped ellipse (0°) nozzle geometries as *Re* increases. This is based on the different flow patterns observed between the two jet geometries near the impingement region, which is the region of the highest heat transfer coefficient. The focusing effect discussed previously, increases in the downstream direction of flow because of the increase in the crossflow, which strengthens the upstream wall vortex. The axis switching process is believed to interact with this vortex in such a way as to increase the velocity and, therefore, the impingement heat transfer near the impingement region. This in turn increases the surface averaged heat transfer rate, as indicated in the results of Fig. 14. It is not clear why this effect is more pronounced in the uniform heat flux boundary condition case. This may be a result of the local near wall temperature distribution. The constant heat flux boundary condition has a greater temperature slope near the wall, by virtue of its greater heat transfer rate, which may be more sensitive to the flow enhancement caused by the cusped ellipse jet.

In summary, the cusped ellipse jets demonstrate a 13–20% increase in discharge flow coefficient compared with the circular jet discharge flow coefficient. The heat transfer data show a similar pattern when compared with the surface flow pattern. Regions of high jet-to-jet and jet-to-crossflow interaction correspond to regions of low heat transfer. These regions are distorted in the streamwise direction as the crossflow effects increase. Moving downstream, the interaction of the crossflow increases and creates larger and larger surface vortices at the surface associated with a more intense vorticity field. This interaction, in the case of the cusped ellipse (0°) jets, results in a focusing of the flow streamlines at the impingement point and could be a reason for improved heat transfer. The heat transfer rate is a maximum at the stagnation points, but the magnitudes of the peaks decay along the crossflow direction. This decay appears to be less significant for the cusped ellipse (0°) due to the focusing of the jet near impingement. The uniform heat flux boundary condition case results in higher *Nu* values compared to the isothermal case for both jet geometries. The cusped ellipse jet shows a higher sensitivity to H/D_H. The cusped ellipse (0°) geometry behaves as the circular jet geometry for the isothermal surface case, but for the uniform heat flux surface case, the cusped ellipse (0°) geometry has a higher *Nu* than the circular jet geometry.

4. Conclusions

The aim of this study is to investigate the flow and heat transfer characteristics of confined jet array impingement with crossflow. Two different orifice geometries were studied and the effects of *Re* and *H*/*D* are assessed. It was found that the cusped ellipse (0°) jets affects the near surface region and increases the overall heat transfer for the uniform heat flux boundary condition, particularly at high *Re* conditions. The crossflow effects are shown to influence the heat transfer results based on the interaction with the jet impingement. It is recommended that further studies investigate the reason for the observed sensitivity of the heat transfer to the thermal boundary conditions and that more detailed three-dimensional flow studies be carried out to study the vortex interactions with the crossflow. Furthermore, a study of other orifice geometries may results in increases in heat transfer, under appropriate flow conditions.

References

[1] R.J. Margason, Fifty Years of Jet in Cross Flow Research, AGARD CP-534, 1993.
[2] B. Han, R.J. Goldstein, Jet-impingement heat transfer in gas turbine systems, Ann. N.Y. Acad. Sci. 934 (2001) 147–161.
[3] J.W. Baugh, S. Shimizu, Heat transfer measurement from a surface with uniform heat flux and an impinging jet, Trans. ASME J. Heat Transfer 111 (1989) 1096–1098.
[4] M.S. El-Genk, L. Huang, Z. Guo, in: R.S. Pate, M.K. Jenen (Eds.), Heat Transfer Between a Square Flat Plate and a Perpendicularly Impinging Circular Air Jet, HT-202, ASME, NY, San Diego, CA, Aug 9–12, 1992, pp. 33–38.
[5] C.H. Huang, J.Y. San, M.H. Shu, Impingement cooling of a confined circular air jet, Int. J. Heat Mass Transfer 40 (6) (1997) 1355–1364.
[6] M. Angioletti, R.M. Di Tommaso, E. Nino, G. Ruocco, Simultaneous visualization of flow field and evaluation of local heat transfer by transitional impinging jets, Int. J. Heat Mass Transfer 46 (2003) 1703–1713.
[7] P. Hrycak, Heat transfer from round impinging jets to a flat plate, Int. J. Heat Mass Transfer 26 (12) (1983) 1857–1865.
[8] L.W. Florschuetz, Y. Isoda, Flow distributions and discharge coefficient effects for jet array impingement with initial crossflow, Trans. ASME 105 (1983) 296–304.
[9] J.M.M Barata, D.F.G. Durao, M.V. Heitor, Velocity characteristics of multiple impinging jets through a crossflow, J. Fluid Eng. 114 (1992) 231–239.
[10] J.M.M Barata, Fountain flows produced by multiple impinging jets in a crossflow, AIAA J. 34 (12) (1996) 2523–2530.
[11] A. Benard, L.E. Brizzi, J.L. Bousgarbies, Study of several jets impinging on a plane wall: visualizations and laser velocimetry investigations, J. Fluid Eng. 121 (1999) 808–812.
[12] C. Camci, K. Kim, S.A. Hippensteele, A new hue capturing technique for the quantitative interpretation of liquid crystal images used in convective heat transfer studies, J. Turbomach. 114 (4) (1992) 765–775.

[13] S.A. Hippensteele, L.M. Russell, F.S. Stepka, Evaluation of a method for heat transfer measurements and thermal visualization using a composite of heater element and liquid crystals, Trans. ASME J. Heat Transfer 105 (1) (1983) 184–189.

[14] S.A. Hippensteele, L.M. Russell, F.J. Torres, Local heat transfer measurement on a large-scale model turbine blade airfoil using a composite of a heater element and liquid crystal, J. Eng. Gas Turbines Power 107 (4) (1985) 953–960.

[15] M. Parsley, The use of thermochromic crystal in heat transfer and flow visualization research, in: Second International Symposium on Fluid Visualization, 1998.

[16] K.W. Van Treuren, Z. Wang, P.T. Ireland, T.V. Jones, Detailed measurements of local heat transfer coefficient and adiabatic wall temperature beneath an array of impinging jets, Trans. ASME J. Turbomach. 116 (3) (1994) 369–374.

[17] Z. Wang, P.T. Ireland, T.V. Jones, An advanced method of processing liquid crystal video signals from transient heat transfer experiments, ASME Paper No. 93-GT-282, 1993.

[18] Z. Wang, P.T. Ireland, T.V. Jones, R. Davenport, A colour image processing system for transient liquid crystal heat transfer experiments, ASME Paper No. 94-GT-290, 1994.

[19] T. T. Hamadah, Impingement cooling of a simulated electronic package with a square array of round air jets, in: National Heat Transfer Conference 1989, pp. 107–112.

[20] A.M. Huber, R. Viskanta, Effect of jet–jet spacing on convective heat transfer to confined, impinging arrays of axisymmetric air jets, Int. J. Heat Mass Transfer 37 (18) (1994) 2859–2869.

[21] V.P. Schroeder, S.V. Garimella, Heat transfer in the confined impingement of multiple air jets, in: Proceedings of 1998 ASME International Mechanical Engineering Congress and Exposition, Anaheim, CA, 1998.

[22] N.T. Obot, T.A. Trabold, Impingement Heat Transfer Within Arrays of Circular Jets. Part 1: Effects of Minimum, Intermediate, and Complete Crossflow for Small and Large Spacings, Trans. ASME 109 (1987) 872–879.

[23] D.E. Metzger, Heat transfer in gas turbine engines, Winter Annual Meeting of The American Society of Mechanical Engineers, Boston, Massachusetts, Vol. 87, December 13–18, 1987.

[24] D.-H. Rhee, P.-H. Yoon, H.H. Cho, Local heat/mass transfer and flow characteristics of array impinging jets with effusion holes ejecting spent air, Int. J. Heat Mass Transfer 46 (2003) 1049–1061.

[25] Y. Huang, S.V. Ekkad, J.-C. Han, Detailed heat transfer distributions under an array of orthogonal impinging jets, J. Thermophys. Heat Transfer 12 (1) (1998) 73–79.

[26] J.A. Parsons, J.-C. Han, Rotation effect on jet impingement heat transfer in smooth rectangular channels with heated target walls and radially outward cross flow, Int. J. Heat Mass Transfer 41 (13) (1998) 2059–2071.

[27] G. Failla, E.H. Bishop, J.A. Liburdy, Enhanced jet impingement heat transfer with crossflow at low Reynolds numbers, J. Electron. Manuf. 9 (2) (1999) 167–178.

[28] S.J. Lee, J.H. Lee, D.H. Lee, Local heat transfer measurements from an elliptic jet impinging on a flat plate using liquid crystal, Int. J. Heat Mass Transfer 37 (6) (1994) 967–976.

[29] R. Owens, J.A Liburdy, Effect of nozzle geometry on the heat transfer distribution in a jet array, in: ASME National Heat Transfer Conference, 1995.

[30] S.C. Arjocu, J.A. Liburdy, M.M. Ferland, Effects of orifice geometry on the heat transfer distribution for impinging jet array, in: Proceedings of the ASME Heat Transfer Division, 3, 1997, pp. 47–54.

[31] S.C. Arjocu, J.A. Liburdy, Near surface characterization of an impinging elliptical jet array, J. Fluid Eng. 121 (1999) 384–390.

[32] S.C. Arjocu, J.A. Liburdy, Identification of dominant heat transfer modes associated with the impingement of an elliptic jet array, J. Heat Transfer 122 (2000) 240–247.

[33] B.P.E. Dano, Flow Characteristics of Semi-Confined Impinging Jet Arrays, MS Thesis, Oregon State University, Corvallis, OR, 2000.

[34] K. Kanokjaruvijit, Effects of Orifice Geometry and Boundary Surface Condition on Heat Transfer of Impinging Jet Array, MS Thesis, Oregon State University, Corvallis, OR, 1999.

[35] W.F. Kays, Convective Heat Transfer, McGraw-Hill Pub., NY, 1966.